ELSEVIER

Contents lists available at ScienceDirect

## **Materials Today Physics**

journal homepage: https://www.journals.elsevier.com/ materials-today-physics



# Metamorphosis of three-dimensional kirigami-inspired reconfigurable and reprogrammable architected matter



Yanbin Li, Jie Yin\*

Department of Mechanical and Aerospace Engineering, North Carolina State University, Raleigh, NC, 27695, USA

#### ARTICLE INFO

Article history:
Received 31 May 2021
Received in revised form
23 August 2021
Accepted 23 August 2021
Available online 25 August 2021

Keywords: Three-dimensional kirigami Architected materials Kinematic bifurcation Reconfigurability Reprogrammability

#### ABSTRACT

Most shape-morphing materials are limited to one-to-one shape-changing process, i.e., one design corresponds to one target shape, thus it is hard to be reshaped due to the constraint of limited mobilities (degrees of freedom). Here, we propose harnessing kinematic bifurcation in mechanisms with multiple branched transformation paths to achieve enhanced reconfigurability and shape reprogrammability in a new class of three-dimensional (3D) kirigami-inspired architected matter. The reconfigurable and reprogrammable architected matter is constructed from planar tessellation of 3D kirigami-inspired transformable modules. The module consisting of eight closed-loop connected cubes exhibits both 3D non-bifurcated and bifurcated transformation modes, the motions of which are well captured by the developed kinematics model. The modules can be periodically tessellated in plane to form a flat, thick panel in both a diluted (with voids) and compact (without voids) pattern with multiple encoded, compatible transformation modes. Consequently, it can undergo a series of consecutive shape changes by reconfiguring into varieties of 3D transformable architectures that are conceptually in analogy to metamorphosis in some living organisms during growth. The endowed rich mobilities are found to derive from the kinematic bifurcation. Among them, a unique transformed 3D architecture can be further reprogrammed to reconfigure into multiple architected shapes with zero and non-zero Gaussian curvature through both forward and inverse designs. Such 3D reconfigurable kinematic matter is attractive for potential applications in reconfigurable metamaterials and morphing architectures.

© 2021 Elsevier Ltd. All rights reserved.

#### 1. Introduction

The architecture of living or artificial matter is crucial for their properties and functionalities. Some living systems such as animals and microorganisms undergo a series of abrupt shape transformation during their developmental stages to adapt to different living environments. Such a biological evolution process of shape changes in form and structure is named metamorphosis. Similar artificial metamorphic materials and structures that are capable of changing their geometries and architectures have recently attracted growing interest due to shape changing imparted rich new properties and functionalities [1–4]. Such metamorphic materials have found broad applications in reconfigurable metamaterials [5], self-reconfigurable robots [6], morphing aerostructures [7], and four-dimensional (4D) printing [8].

The ancient paper art of origami and kirigami [9,10] provides

\* Corresponding author. E-mail address: jyin8@ncsu.edu (J. Yin). unique ways to design metamorphic materials via folding in origami and cutting/folding in kirigami with demonstrated broad applications in engineering [11–23]. Starting from a thin flat sheet with prescribed creases in origami, it can rigidly fold into virtually any 3D shape [24]. Similarly, a thin flat sheet with cut patterns (slits or holes) in kirigami can morph into desired expanded 2D shapes [15,25,26] or 3D pop-up structures [27,28]. Reversely, inverse design of crease or cut patterns can be prescribed to fit target surface morphologies with intrinsic curvature [27,29].

Mathematically, both 2D and 3D shape shifting can be considered as a one-to-one mapping, i.e., one certain crease or cut pattern corresponds to one target shape, thus, once morphed, normally it is challenging to be reprogrammed into other different shapes. To enhance its reconfigurability, one can design pluripotent crease patterns in origami [30] or combine cutting and folding in kirigami thin sheets [16,31], where the same crease or cutting pattern could transform into multiple 3D configurations through combinatorial folding [16,23,30,31], i.e., one-to-multiple mapping. Beyond conventional 2D thin sheet-based origami and kirigami [9], designing

3D origami and kirigami-inspired modules with multiple deformation modes provides a promising way to construct 3D reconfigurable architected materials with enhanced reconfigurability [32–35]. Recent studies demonstrate that space-filling tessellation of 3D polyhedral origami-inspired modules creates 3D prismatic architected materials that can reconfigure into multiple 3D structural modes via internal mechanism [33]. Very recently, we demonstrate utilizing the complementary shapes between reconfigurable 3D kirigami modules to design multi-dimensional architected materials that can be disassembled and re-assembled for programmable properties [35]. Despite the advance, the shape changes in such 3D reconfigurable materials follow the stable equilibrium folding paths with limited mobilities (degrees of freedom) [16,23,32–35].

Beyond equilibrium motion, bifurcation provides an effective way to generate multiple shape transformation with branched transition paths in engineering systems when independent variants reach critical values [36], for instance, the bifurcation of Euler's Elastica rod can lead to multiple deformed shapes [37]. Notably, bifurcation often occurs in the kinematic deployment of rigid mechanisms composed of rotatable joint hinges and bar links [38], i.e., kinematic bifurcation. For a bifurcated rigid mechanism, when the rotating angles of its joint hinges reach a critical value, its configuration transformation can deviate from its original equilibrium path and branch into distinct kinematic deployment path(s) at the bifurcation point [39], which provides more design space for enhanced structural transformation. In comparison, the nonbifurcated (equilibrium) rigid mechanism will transform its shapes by following certain equilibrium paths with less mobilities during reconfiguration. Naturally, it provokes the question of whether one can harness kinematic bifurcation to unleash their full potential in generating rich structural reconfigurations in 3D origami/kirigami module-inspired reconfigurable materials.

Here, we explore the potential of leveraging kinematic bifurcation [40] for enhancing both reconfigurability and reprogrammability in an example system of 3D kirigami-inspired architected matter. As illustrated in Fig. 1A, inspired by the thin sheet-based kirigami approach [15,25,26] and the toy of infinity cube or flexicube [41], we construct 3D kirigami modules by cutting bulk materials with non-negligible thickness into a closed-loop connection of a different number of cubes [15,35]. We explore the kinematics of the closed-loop mechanism-based 3D kirigami-inspired modules. We find that the eight cube-based kirigami module shows the highest level of reconfigurability by transforming into more distinct 3D shapes, arising from the kinematic bifurcation (Fig. 1B). Through

rational planar tiling technique to satisfy the compatible deformation among units, we assemble the kirigami modules in plane to construct quasi-3D kinematic architected matter in the form of a flat, thick panel (Fig. 1C). We find that such planar structures can undergo both encoded non-bifurcated and bifurcated kinematic transitions to reconfigure into varieties of 3D transformable architectures (Fig. 1D), the consecutive shape changes of which are conceptually in analogy to metamorphosis in living matter [42,43] that involves evolutionary shape changes in form and structure during growth. We further find that a unique reconfigured architecture can act as a pluripotent platform for further reprogramming and re-evolving into architected curved surface morphologies (Fig. 1E).

#### 2. Results

#### 2.1. Construction of 3D kirigami-inspired reconfigurable modules

Inspired by the classical square cut pattern in thin sheets with orthogonal slits [15,25,26] and the toy of infinity cube or flexicube [41], we extend the conventional kirigami approach in thin sheets to bulk materials with non-negligible thickness [15,35]. Fig. 2A-C and Fig. S1a demonstrate a generalized way to construct 3D kirigami-inspired modules by cutting a cuboidal-shaped bulk material into connected cubes that form a looped mechanism [35]. Consequently, the orthogonal line cuts (slits), planar square-shaped cut units, and point joint hinges in the conventional 2D kirigami approach [15,25,26] are replaced by the orthogonal plane cuts, 3D cube units, and line hinges (highlighted in dark green bar) in the extended 3D kirigami approach [35], respectively. Depending on the number of introduced plane cuts and cut locations, it can generate different types of modules consisting of 4 (Figs. 2A), 6 (Fig. 2B), and 8 cubes (Fig. 2C-E). Each rigid cube can be simplified as a linkage and is connected through elastic torsional hinges to form a looped rigid mechanism. It allows 3D transformation of cubes around the hinges into different configurations. Thus, it could potentially render more degrees of freedom than the conventional thin sheets-based 2D kirigami approach [15,25,26].

The three 3D kirigami-inspired modules consisting of 4, 6, and 8 cubes can be modeled as a 4R (rotational), 6R, and 8R looped rigid mechanism, respectively. Their motions can be characterized by the dihedral angle  $\gamma_{ij}$  between the counterclockwise-ordered neighboring cube i and cube j shown in Fig. 2. Generally, the motion can be categorized into three kinematic transition modes in terms of the number of rotated hinge pair(s) involved during

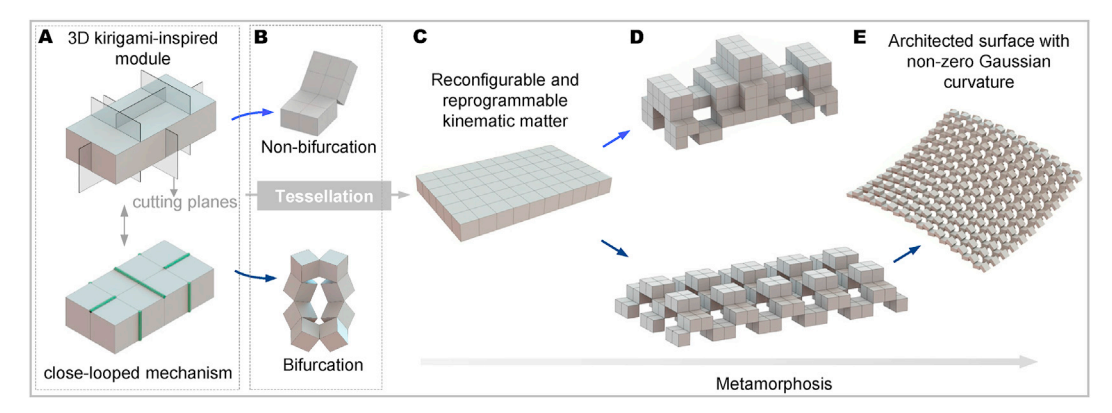


**Fig. 1.** Schematics on the construction of 3D kirigami-inspired reconfigurable and reprogrammable kinematic matter with its shape transformation from a quasi-3D form to 3D architectures and curved surfaces via both non-bifurcated and bifurcated modes. (**A**) cube-based 3D kirigami-inspired module in a close-looped mechanism. (**B**) Non-bifurcated (top) and bifurcated (bottom) shape transformation in the module. (**C-E**) In-plane tessellation of 3D modules forms a quasi-3D kinematic matter (**C**) and its metamorphosis of reconfiguring into varieties of 3D architectures (**D**) and architected surface with non-zero Gaussian curvature (**E**).

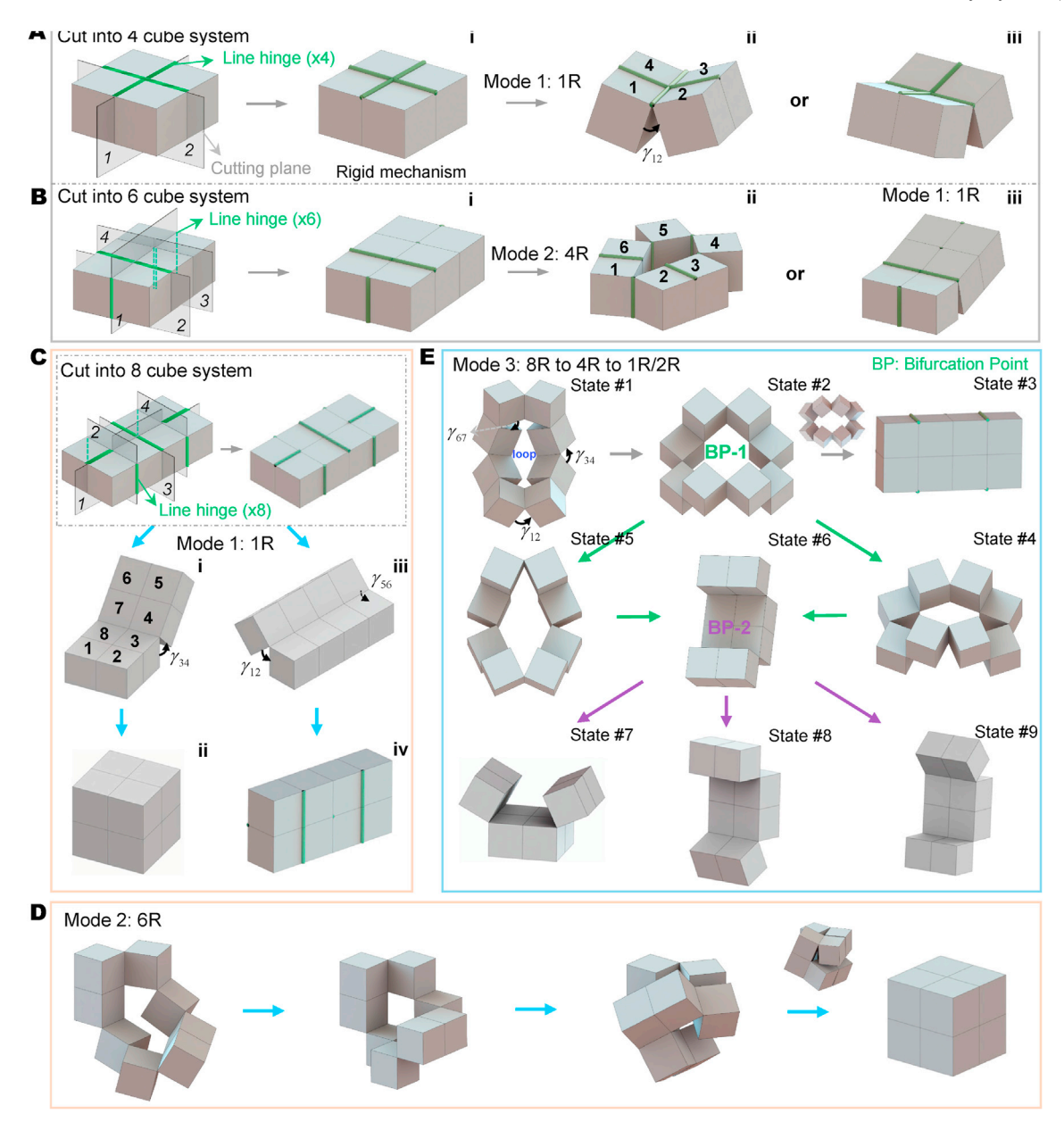


**Fig. 2.** Construction of 3D kirigami-inspired transformable modules through generalized plane cutting. (**A-C**) Schematic illustration of generating 4-cube (**B**), and 8-cube modules (**C**) by introducing 2, 4, and 4 cutting planes to cuboidal bulk materials. Each cube act as a linkage and is connected through elastic torsional line hinges to form a rigid mechanism. (**C–E**) Three kinematic transformation modes in 8-cube module: Mode 1 in (**C**) with one rotational (1R) linkage mechanism; Mode 2 in (**D**) with 6R linkage mechanism; and Mode 3 in (**E**) with 8R linkage mechanism. Only Mode 3 exhibits kinematic bifurcation with two demonstrated bifurcation points when transforming from configuration State #1 to State #9.

### reconfiguration.

- (1) Mode 1 with 1R linkage mechanism in all the three modules (Fig. 2A (ii-iii), Fig. 2B (iii), and Fig. S1b), where their motion can be described by a single non-zero dihedral angle  $\gamma$ , while all other angles are zero, e.g.,  $\gamma_{12}=\gamma_{34}=\gamma$  in Fig. 2A (ii),  $\gamma_{23}=\gamma_{61}=\gamma$  in Fig. 2B (ii), and  $\gamma_{12}=\gamma_{56}=\gamma$  in Fig. 2C (iii). It undergoes monotonic shape changes, and the plane cuts remain closed during motion.
- (2) Mode 2 with 4R linkage mechanism in the 6-cube module (Fig. 2B) and 6R linkage mechanism in the 8-cube module (Fig. 2D and Fig. S1C), where only two dihedral angles are kept as zero during motion, e.g.,  $\gamma_{23}=\gamma_{61}=0$  in Fig. 2B (ii) and  $\gamma_{23}=\gamma_{67}=0$  in Fig. 2D, while all other angles are non-

- zero. The plane cuts are opened to form a 3D void during motion.
- (3) Mode 3 with 8R linkage mechanism (Fig. 2E and Fig. S1c) in the 8-cube module, where all the plane cuts are opened, and all the eight dihedral angles become non-zero during motion.

We note that Mode 1 and Mode 2 are stable transition modes by following the 1R or 6R motion path without bifurcation. By contrast, Mode 3 undergoes multiple consecutive kinematic bifurcations. It exhibits alternative transition pathways at the bifurcated points shown in Fig. 2E. For example, when it transforms from configuration State #1 to State #3, it preserves the looped 8R linkage and shows no bifurcation. However, the intermediate

configuration State #2 with  $\gamma_{12}=90^\circ$  is a critical state, which represents the first bifurcation point (BP-1). It can branch into two alternative bifurcated transition paths by transforming from original 8R linkage (State #2) to a reduced 4R linkage (either State #4 or State #5). Furthermore, as configuration State #4 or State #5 keeps rotating, it engenders the second bifurcation point (BP-2) at configuration State #6 with a closed pore ( $\gamma_{12}$  or  $\gamma_{34}=180^\circ$ ). State #6 could further bifurcate into three combinatoric kinematic paths to either configuration State #7 or State #8 or State #9 through a further reduced non-looped 2R linkage mechanism. We note that transition Mode 1 in the 8-cube module is similar to the 8 cube-based toy known as a flexicube [41], however, the flexicube shows only chain-like rotations without kinematic bifurcation (Fig. S1a-iii) due to its different hinge locations from our design.

Compared to limited reconfigurability in 4- and 6-cube modules via non-bifurcated transition Mode 1 and Mode 2, the 8-cube module exhibits both non-bifurcated and bifurcated shapemorphing characteristics with versatile transformed configurations (Fig. 2C-E). Thus, in the following, we will focus on the 8 cube-based module and its assembled structures.

#### 2.2. Kinematic analysis

Theoretically, the kinematics of the 3D kirigami module that describes the angle relations during the three transition modes can be captured by the Denavit-Hartenberg rule [44] as

$$\sum_{i=1}^{8} \mathbf{T}_{i(i+1)} = \mathbf{I}$$
 [1]

where  $\mathbf{T}_{i(i+1)}$  (i.e.,  $T_{12}$ ,  $T_{23}$ , ...,  $T_{81}$ ) is the transformation matrix determined by  $\gamma_{ij}$  (Fig. S2) and  $\mathbf{I}$  is the 4 × 4 identity matrix.

For Mode 1, we have  $\gamma_{12}=\gamma_{56}$  for the transition path shown in Fig. 2C (iii-iv), i.e., a linear angle relationship in Fig. 3A. For Mode 2 in Fig. 2D, by setting  $\gamma_{23}=\gamma_{67}\equiv 0$  in Eq. (1), the angle relations can be obtained as (see details in *Supplementary Materials*)

into two additional paths as  $\gamma_{12}$  further increases from 90° to 180°. Consequently, the 8R mechanism becomes a 4R mechanism with a single DOF. Based on Eq. (3), we can readily derive the angle relations in the 4R mechanism as

$$\begin{array}{l} \gamma_{12} = \gamma_{56} = 180^{\circ} - \gamma_{34} \\ \gamma_{34} = \gamma_{78}, \gamma_{23} = \gamma_{45} = \gamma_{67} = \gamma_{81} = 90^{\circ} \end{array} \tag{4}$$

Fig. 3B shows that when  $\gamma_{34}$  increases from  $90^\circ$  to  $180^\circ$  in the 4R mechanism, it corresponds to one transition path that bypasses configuration State #4 (see the green line in Fig. 3B), while a decreasing  $\gamma_{34}$  from  $90^\circ$  to  $0^\circ$  corresponds to the other transition path that bypasses configuration State #5 (see the blue line in Fig. 3B). When  $\gamma_{34}$  reaches  $0^\circ$  or  $180^\circ$ , it encounters another bifurcation point (i.e., BP-2 in Figs. 3B and 2E), where the bifurcated 4R mechanism further reduces to a 2R chain-like mechanism with two DOFs. Fig. 3B shows the corresponding angle changes of the two transition paths as a variation of  $\gamma_{23}$  when transforming from configuration State #6 to State #7 (see the purple line) or to State #8 or State #9 in Fig. 2E.

#### 2.3. Kinematic bifurcation

Next, we utilize the singular value decomposition (SVD) method [45] to predict the demonstrated kinematic bifurcation features. Given its sole rotational motion, we can decompose the transformation matrix **T** into

$$\mathbf{T} = \mathbf{T}_I \mathbf{T}_{\gamma} \tag{5}$$

where  $\mathbf{T}_L$  and  $\mathbf{T}_{\gamma}$  represent the rotation and translation matrix with a constant form (see details in *Supplementary Materials*), respectively. To capture the bifurcation points, we first introduce a numerical perturbation to the dihedral angle  $\gamma_{ij}$  with an infinitesimal increment  $\delta \gamma_{ij}$ . Then, we rewrite  $\mathbf{T}_{\gamma}$  through the Taylor expansion as

$$\mathbf{T}_{ij}^{\gamma_{ij}+\delta\gamma_{ij}} = \mathbf{T}_{ij}^{\gamma_{ij}} + \left(\mathbf{T}_{ij}^{\gamma_{ij}}\right)'\delta\gamma_{ij}$$
 [6]

$$\begin{split} &\gamma_{12} = \gamma_{34} = \gamma_{56} = \gamma_{78} \\ &\gamma_{45} = \gamma_{81} = \arcsin \left[ \sin^2 \gamma_{12} \middle/ \left( 1 + \cos^2 \gamma_{12} \right) \right] \, \left( 0^o \le \gamma_{12} \le 90^o \right) \\ &\gamma_{45} = \gamma_{81} = 180^o - \arcsin \left[ \sin^2 \gamma_{12} \middle/ \left( 1 + \cos^2 \gamma_{12} \right) \right] \, \left( 90^o \le \gamma_{12} \le 180^o \right) \end{split} \tag{2}$$

Eq. (2) shows that Mode 2 has a single DOF of  $\gamma_{12}$ , where  $\gamma_{45}$  increases nonlinearly with  $\gamma_{12}$  (Fig. 3A).

Compared to Mode 1 and 2, Mode 3 demonstrates more intriguing kinematics with multiple bifurcation points shown in Figs. 2E and 3B. When transforming from configuration State #1 to State #3, the opening of cuts through the 8R-looped mechanism shows a single DOF motion with their angle relations given by

$$\begin{array}{l} \gamma_{12} = \gamma_{34} = \gamma_{56} = \gamma_{78} \, \left(0^o \leq \gamma_{12} \leq 90^o\right) \\ \gamma_{23} = \gamma_{45} = \gamma_{67} = \gamma_{81} = arcsin[(1-cos \, \gamma_{12})/(1+cos \, \gamma_{12})] \end{array} \label{eq:gamma_3} \tag{3}$$

The results are plotted as the black curve in Fig. 3B. It shows that as  $\gamma_{12}$  increases from  $0^\circ$  to  $90^\circ$  (cuts opening) and then decreases to  $0^\circ$  (cuts closing),  $\gamma_{23}$  increases monotonically from  $0^\circ$  to  $180^\circ$ . However, at  $\gamma_{12}=90^\circ$ , i.e., configuration State #2, the original path in the 8R-looped mechanism bifurcates (see BP-1 in Figs. 3B and 2E)

where  $(\mathbf{T}_{ij}^{\gamma_{ij}})' = \partial \mathbf{T}_{ij}^{\gamma_{ij}}/\partial \gamma_{ij}$  and the higher-order terms are neglected (see details in *Supplementary Materials*). Thus, combining Eqs. [1], [5] and [6], we have (see details in *Supplementary Materials*)

$$\prod_{i=1}^{8} \mathbf{T}_{i(i+1)}^{L} \mathbf{T}_{i(i+1)}^{\gamma_{i(i+1)}} + \sum_{i=1}^{8} \mathbf{M}_{i} \delta \gamma_{i(i+1)} = \mathbf{I}$$
 [7]

where  ${\bf M}$  is the coefficient matrix, which can be decomposed using the SVD method into

$$\mathbf{M} = \mathbf{U}\mathbf{V}\mathbf{W}^{\mathrm{T}}$$
 [8]

where **U** and **W** are  $6 \times 6$  and  $8 \times 8$  square orthogonal matrices containing the left- and right-singular vectors, respectively. V is a  $6 \times 8$  rectangular matrix with r non-zero singular values on its main diagonal, where r is the rank of the matrix **M**.

Numerically monitoring the zero values of the six singular

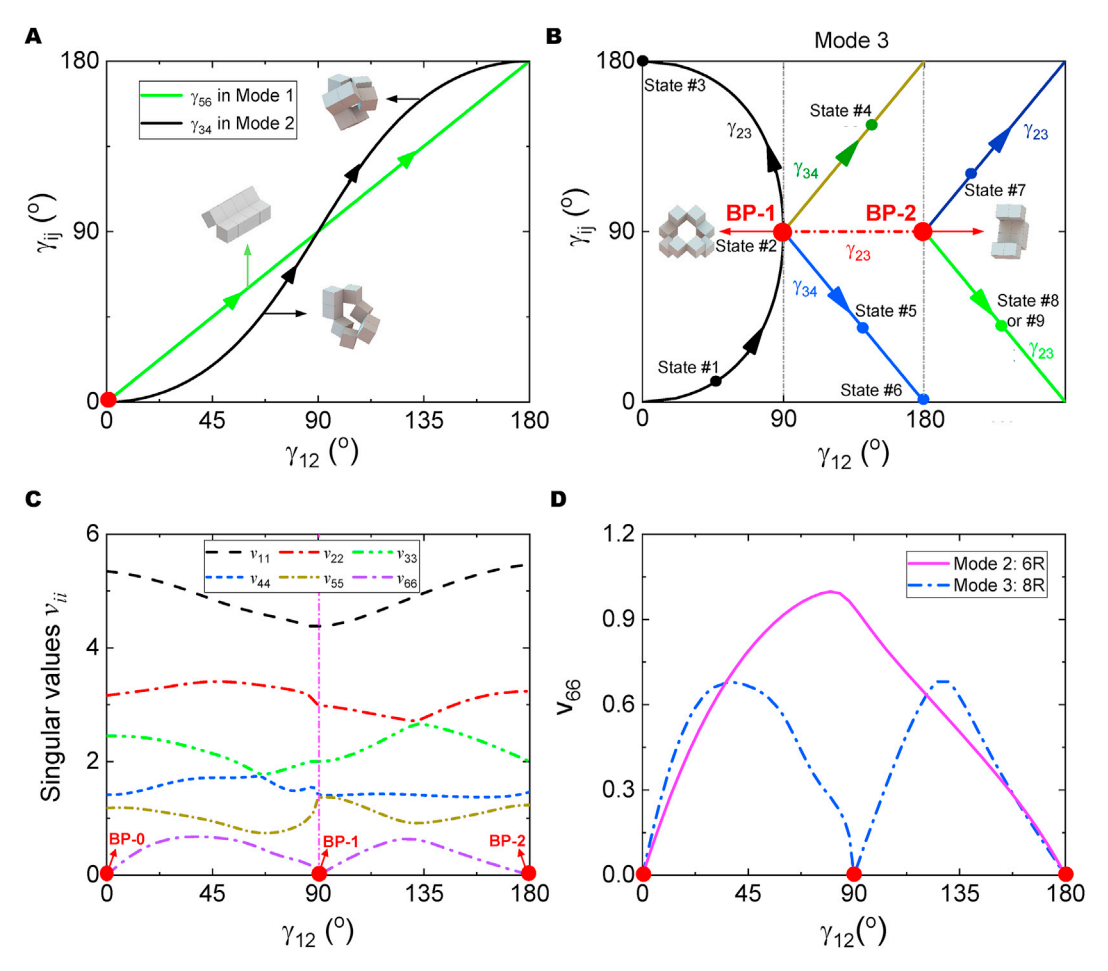


**Fig. 3.** Kinematic analysis of 8-cube module. (**A**, **B**) Kinematic paths defined as dihedral angle relations during its transformation in Mode 1 and Mode 2 (A), and Mode 3 (B). (**C**) Variations of six singular values  $v_{ii}$  during transformation Mode 3. (**D**) Comparison of the sixth singular value  $v_{66}$  between Mode 2 and Mode 3.

values  $v_{kk}$  (k=1,2,...,6) of the matrix **V** predicts the locations of bifurcation points of the 3D kirigami module. Fig. 3C and Fig. S3 show the presence of three predicted bifurcation points (BP-0, BP-1, and BP-2) located at  $\gamma_{12}=0^\circ$ , 90°, and 180° when the sixth singular value  $v_{66}$  is equal to zero, i.e.,  $v_{66}=0$ . Kinematically, BP-0 represents the three potential transition modes (i.e., Mode 1 to Mode 3 in Fig. 2C-E), while BP-1 and BP-2 are the bifurcation points as demonstrated in Mode 3. We further compare the variation of  $v_{66}$  in Mode 2 with 6R mechanism and Mode 3 with 8R mechanism in Fig. 3D. It shows that no bifurcation occurs in Mode 2 when  $0^\circ < \gamma_{12} < 180^\circ$ , which is consistent with the demonstration in Fig. 2D.

# 2.4. Design of '-' and '+' -shaped building blocks with preserved kinematics

Next, we assemble the reconfigurable modules as units in a periodic way to form reconfigurable quasi-3D architected matter through in-plane tiling. It should be noted that periodic tiling of the units is non-trivial and rather challenging, considering (1) the out-of-plane transformation in the 8R linkage, (2) compatible kinematic motions to avoid structural frustrations, and (3) encoding rich shape-morphing features from the base unit without sacrificing its intrinsic multiple kinematic non-bifurcated and bifurcated modes.

To address the challenge, we design two types of building blocks in the "-" (Fig. 4A) and "+" (Fig. 4B) shapes that will be used for constructing reconfigurable architected matter with compatible,

preserved transformation modes. Merging the overlapped cubes between the base unit (center) and its transformed shapes (configuration State #3 in Mode 3) uni-axially and bi-axially generates the "— "- and "+ "-shaped building blocks, respectively (see details on the hinge distribution in Fig. S4a). To experimentally explore their transformation, we fabricate the prototypes of the cube modules using 3D printing (Convex Objet-260) and connect them using ultra-flexible plastic tapes to imitate free-rotational hinges (see details in *Supplementary Materials*).

Fig. 4C–D demonstrate their configuration evolutions through 3D-printed prototypes. To eliminate the potential torsion of their flexible hinges, we also fabricate the prototypes of building blocks made of wooden cubes connected with metal hinges. We find that the kinematic transitions in both 3D-printed and wooden prototypes are consistent with each other (Fig. S4b-S4d and Supplementary Video S1). Remarkably, both building blocks preserve all the three non-bifurcated and bifurcated kinematic transition modes in the base unit without causing structural frustration. Thus, following the three transition modes in the base unit, both building blocks can consecutively reconfigure into a library of distinct 3D transformable architectures (e.g., car, box, stair, building, airplane, and other complex 3D shapes in Fig. 4C-D and Fig. S5-S6). For example, Fig. 4C (i) and Fig. 4D (i) show the transformable architectures via the bifurcated Mode 3 from 8R to 4R and to 2R/1R transformation. Fig. 4C (ii) and Fig. 4D (ii-a) (Type-1) demonstrate the structural reconfigurations via non-bifurcated Mode 1 from 4R to 2R and 1R. Similar structural reconfigurations via non-bifurcated

Y. Li and J. Yin Materials Today Physics 21 (2021) 100511

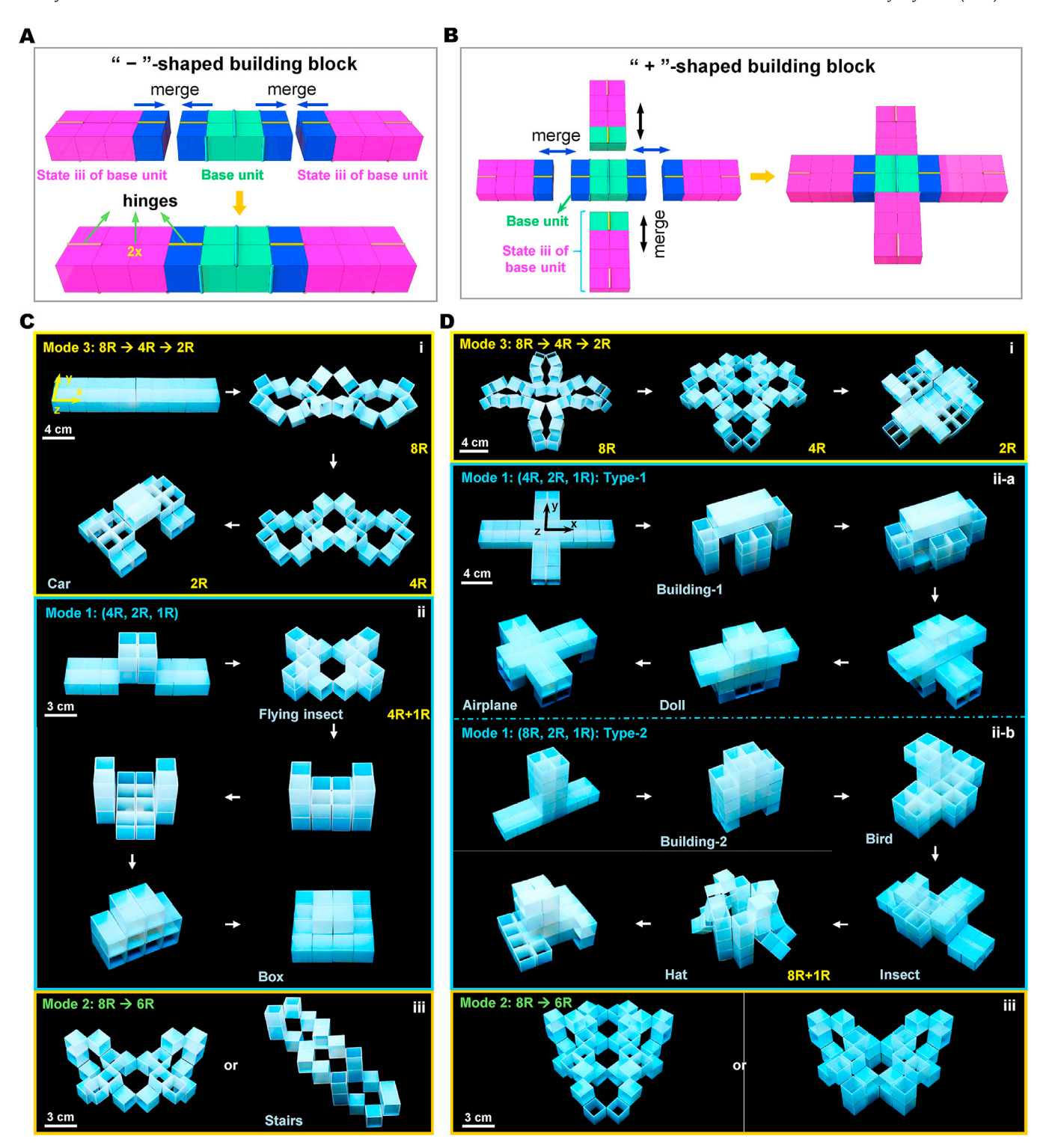


**Fig. 4.** '—' and '+' shaped building blocks and their transformed configurations. (**A, B**) Schematic design details of the '—' and '+' shape building blocks by merging base units and transformed state #3 units uni-axially and bi-axially, respectively. (**C, D**) Prototypes of the two building blocks and their structural reconfiguration by following three basic kinematic transition modes. **C**—*i* and **D**—*i* are based on kinematic transition Mode 3 with kinematic bifurcation, i.e. link number changes from 8R to 4R, finally to 2R/1R; **C**—*iii* and **D**—*iii* correspond to kinematic transition Mode 1 and the transformed configurations are the combinatorics of base unit via 2R and 1R linkage or the 4R linkage in **Fig. 2E**; **C**—*iii* and **D**—*iii* relative to the kinematic transition Mode 2 in **Fig. 2D** with linkage number remaining as 6R.

mode 1 from 8R to 2R and 1R transformation are shown in Fig. 4D (ii-b) (Type-2, Fig. S6a-6b). Fig. 4C (iii) and Fig. 4D (iii) show the reconfigurable architectures via non-bifurcated Mode 2 from 8R to 6R transformation. Specifically, combined transition modes with

additional hinges of overlapping cuboids generates more varieties of shapes. For example, a flying insect (top right of Fig. 4C (ii)) combining 4R (configuration State #4 or #5 of Mode 3 in Figs. 2E) and 1R motion (Fig. 2C (i)); and a hat (Fig. 4D (ii-b)) combining

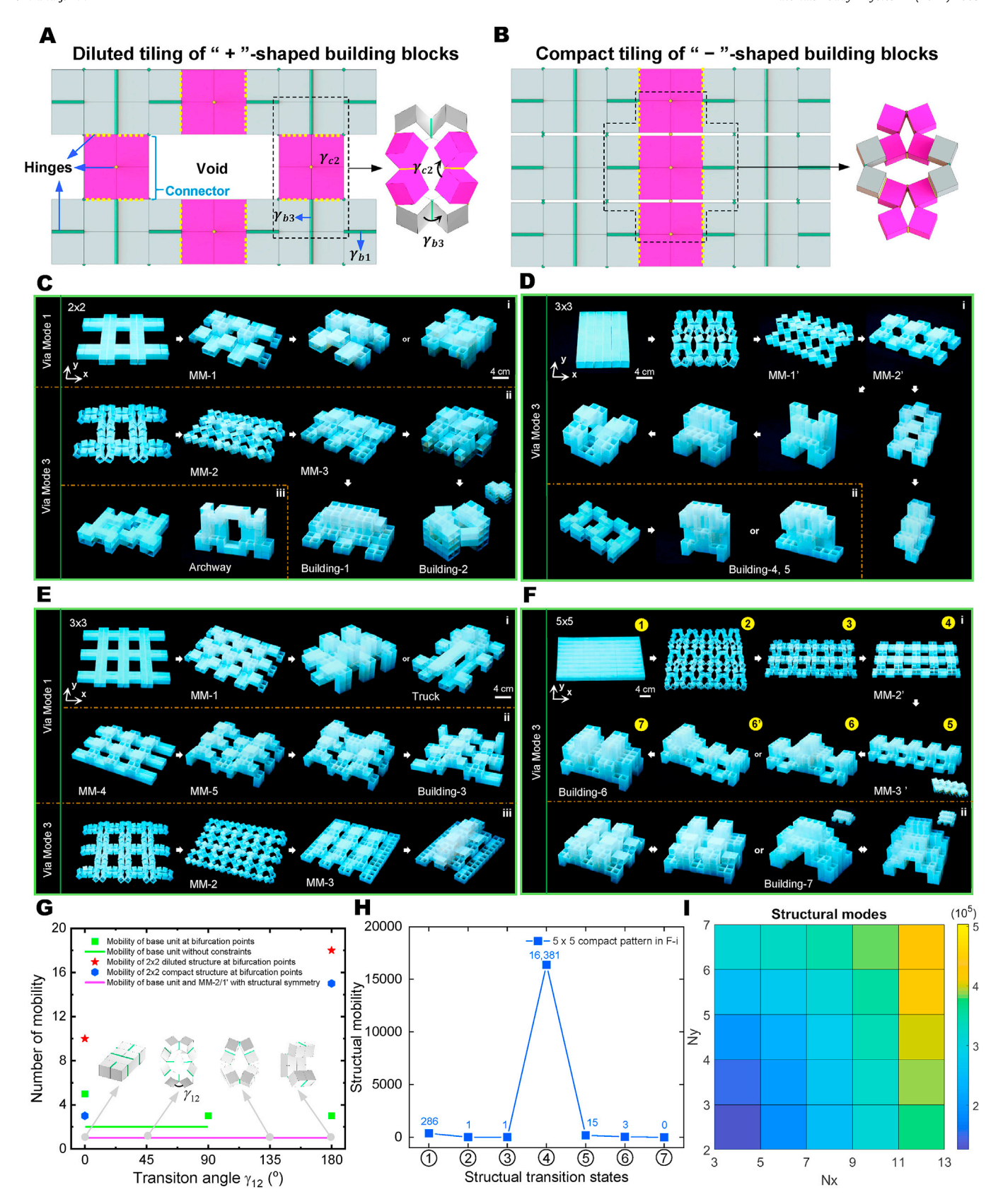


**Fig. 5.** Two tessellated structures through periodic tiling of building blocks in diluted and compact tiling networks. (**A, B**) Schematic design of the planar building blocks and their connection details. (**C**–**F**) Prototypes of reconfigurable 3D periodic materials and non-periodic architectures from the two constructed periodic tiling networks by following different kinematic modes. (**C, E**) Diluted patterns with  $2 \times 2$  and  $3 \times 3$  units. (**D, F**) Compact patterns with  $3 \times 3$  and  $5 \times 5$  units. (**G**) Comparison of kinematic mobilities between the base unit with/without structural symmetry constraint, and the  $2 \times 2$  diluted and compact networks. (**H**) Evolution of the number of structural mobilities in a  $5 \times 5$  compact pattern of (**F**) during its transformation from configuration  $\odot$  to configuration  $\odot$ . (**i**) Combinatoric structural modes of reconfigured MM-2' as shown in **D**-*i* and **F**-*i*.

8R (configuration State #1 in Figs. 2E) and 1R motion (Fig. 2C (iii)). Supplementary video related to this article can be found at https://doi.org/10.1016/j.mtphys.2021.100511

#### 2.5. Metamorphosis of reconfigurable architected matter

Based on the aforementioned "+" and "- "-shaped building blocks, we create two quasi-3D reconfigurable architected matter in the form of a flat, thick panel with periodic diluted (Fig. 5A, with voids) and compact (Fig. 5B, without voids) tiling networks, respectively. Both planar tiling patterns are composed of the base units (highlighted in grey color) and the connectors (configuration State #3 in Mode 3, highlighted in purple color). The design of the connectors is key to ensuring compatible deformation between the connected base units. To avoid geometric frustrations in the compact tiling, we implement two more extra pairs of hinges than the diluted tiling (see its opened state in right of Fig. 5B and hinge details in Fig. S7b). With the tiling design, we note that both periodic networks disable transition Mode 2 of 6R motion in the base unit due to the frustration with its contrary deployment features against the boundaries among the building blocks.

To preserve the kinematic transition Mode 3 of 8R motion from the base unit in Fig. 2E, for the diluted pattern, the dihedral angles  $\gamma_{b1}$  in the base unit and the connector  $\gamma_{c2}$  should satisfy the compatibility condition of

$$\gamma_{b1} + \gamma_{c2} = 180^{\circ} \tag{9}$$

(see the details of  $\gamma_{b1}$  and  $\gamma_{c2}$  in the right of Fig. 5A, Fig. S7a, and Fig. S8a), while for the compact pattern, it needs to overcome the energy barrier (Fig. 5B and Fig. S9a-9b) caused by the twisted bridging hinges with incompatible transformations between the base units and connectors. We note that such geometrical frustration can be readily avoided by sequentially deploying the structures via transition Mode 1 first followed by Mode 3 (Fig. S9c-9d, Supplementary Videos 2 and 3). Thus, both periodic tiling patterns can successfully preserve the primary kinematic features of diverse transition modes and bifurcations from the base unit.

Supplementary video related to this article can be found at https://doi.org/10.1016/j.mtphys.2021.100511

Based on the unique tiling networks, we experimentally demonstrate their shape transformation processes in both diluted (Fig. 5C and E, and Fig. S10) and compact (Fig. 5D and F, and Fig. S11) models of prototypes. To explore the effect of periodicity on the structural reconfigurations, for each tiling pattern, we fabricate two prototypes composed of different numbers of building blocks. Starting from an initial planar configuration, each tiling pattern can consecutively transform into varieties of exclusively 3D sophisticated architectures through the encoded non-bifurcated Mode 1 in Fig. 2C and bifurcated Mode 3 in Fig. 2E. We note that such a shapechanging and evolving process is conceptually in analogy to the biological evolution process of metamorphosis in animals or plants that undergo a series of morphological changes in form and structure during their growth [42,43]. Thus, we borrow the concept of metamorphosis to describe the consecutive transformation from a planar form to varieties of evolving sophisticated architectures in our reconfigurable system.

We classify these transformed 3D configurations into two categories. One is metamorphic materials (MMs) characterized by periodic structures such as MM-1, MM-2, MM-3, MM-4, and MM-5 in the diluted pattern as shown in Fig. 5C ( $2 \times 2$  units) and Fig. 5E ( $3 \times 3$  units), as well as MM-1′, MM-2′, and MM-3′ in the compact pattern as shown in Fig. 5D ( $3 \times 3$  units) and Fig. 5F ( $5 \times 5$  units). We note that the same periodic 3D structures are observed in two prototypes with different numbers of units, e.g., MM-1, MM-2 in

Fig. 5C and E, and MM-1', MM-2' in Fig. 5D and F. The other is non-periodic 3D metamorphic architectures (MAs) with specific topologies such as an archway, a truck, and buildings (Fig. 5C—F), where a larger unit number leads to distinct and more complex architectures. We note that almost all these unique 3D MAs (see more examples in Fig. S10-S11 are morphed from their MMs counterparts by rotating local structural segments. For example, a truck-like shape in Fig. 5E can be achieved by first rotating the boundary segments of MM-1 around the *x*-axis followed by partially deploying *y*-directional structural segments (Fig. S12). Notably, the configurations of MM-3 (Fig. 5C (ii)) and MM-2' (Fig. 5D (i) and Fig. 5F (i)) represent the bifurcation points in Mode 3, which can evolve along multiple branched kinematic paths to generate distinct MMs and MAs.

To quantitatively characterize the preserved kinematic features, we compare the structural kinematic mobilities of Mode 3 (insets of Fig. 5G) among the base unit and  $2 \times 2$  units-based compact and diluted patterns. Fig. 5G shows that the kinematic bifurcations occur consistently at  $\gamma_{12}=0^\circ$ ,  $90^\circ$ , and  $180^\circ$  with dramatically increased mobilities, enabling largely enhanced reconfigurability in the reconfigurable architected matter. It shows that the compact tiling pattern exhibits fewer mobilities than the diluted one due to the structural constraints by the introduced extra bridging hinges.

To quantify the metamorphosis process via bifurcated Mode 3, we use the compact tiling prototype of  $5\times 5$  units as an example to evaluate its mobility evolution during its forward transition from configuration 1 to configuration 2 shown in Fig. 5F. Fig. 5H shows that the initial planar configuration 3 has over 280 potential mobilities due to its bifurcation states. After transforming to configuration 2 and 3 through 8R motion, the number of mobilities dramatically decreases to 1. Remarkably, the following configuration 4 possesses a peak number of over 16,000 mobilities arising from its kinematic bifurcations, which is over 57 times more than its initial state. As it further evolves, the number of mobility dramatically decreases to 3 at configuration 6 and finally reduces to 0 at configuration 7.

The enriched mobilities at configuration 3 (i.e., MM-2' in Fig. 5F) endows a potential enormous space for structural reconfigurability. Given the respective number of independent x- and y-directional rotatable segments  $N_x$  and  $N_y$  in MM-2', it can generate a number of  $2^{N_x+N_y}-3$  combinatoric structural modes  $(N_x, N_y)$  are integers; see Fig. 5I with  $3 \le N_x \le 13$ ,  $2 \le N_y \le 7$  and calculation details in *Supplementary Materials*). For the model with a small number of  $8 \times 8$  units, it can realize over  $10^6$  structural modes with  $N_x = 13$  and  $N_y = 7$ , offering a rich space to accomplish versatile evolving structural reconfiguration.

We note that our kirigami-inspired matter is remarkably different from the reported 3D reconfigurable modular architected materials in terms of their tessellated forms and deformation modes [32–35,46]. Unlike the previously reported periodic spacefilling tessellation of 3D unit cells along all the three directions for constructing reconfigurable materials [32-35,46], the units in our materials are tessellated only in plane to form a quasi-3D reconfigurable material in a planar form but with non-negligible thickness. Consequently, it results in distinct reconfiguration mechanisms and deformation modes. Unlike the 3D-to-3D shape transformation via internal mechanism in prismatic architected materials [33] or soft deformation modes in textured metamaterials [46], our system achieves the quasi-3D-to-3D architecture transformation via distinct closed-loop mechanisms. More importantly, the deformation modes in the reported 3D architected materials fall into the category of non-bifurcated modes with limited reconfigurability [32-35,46], whereas our system harnesses both non-bifurcated and bifurcated kinematic modes for achieving more varieties of structural transformation in 3D.

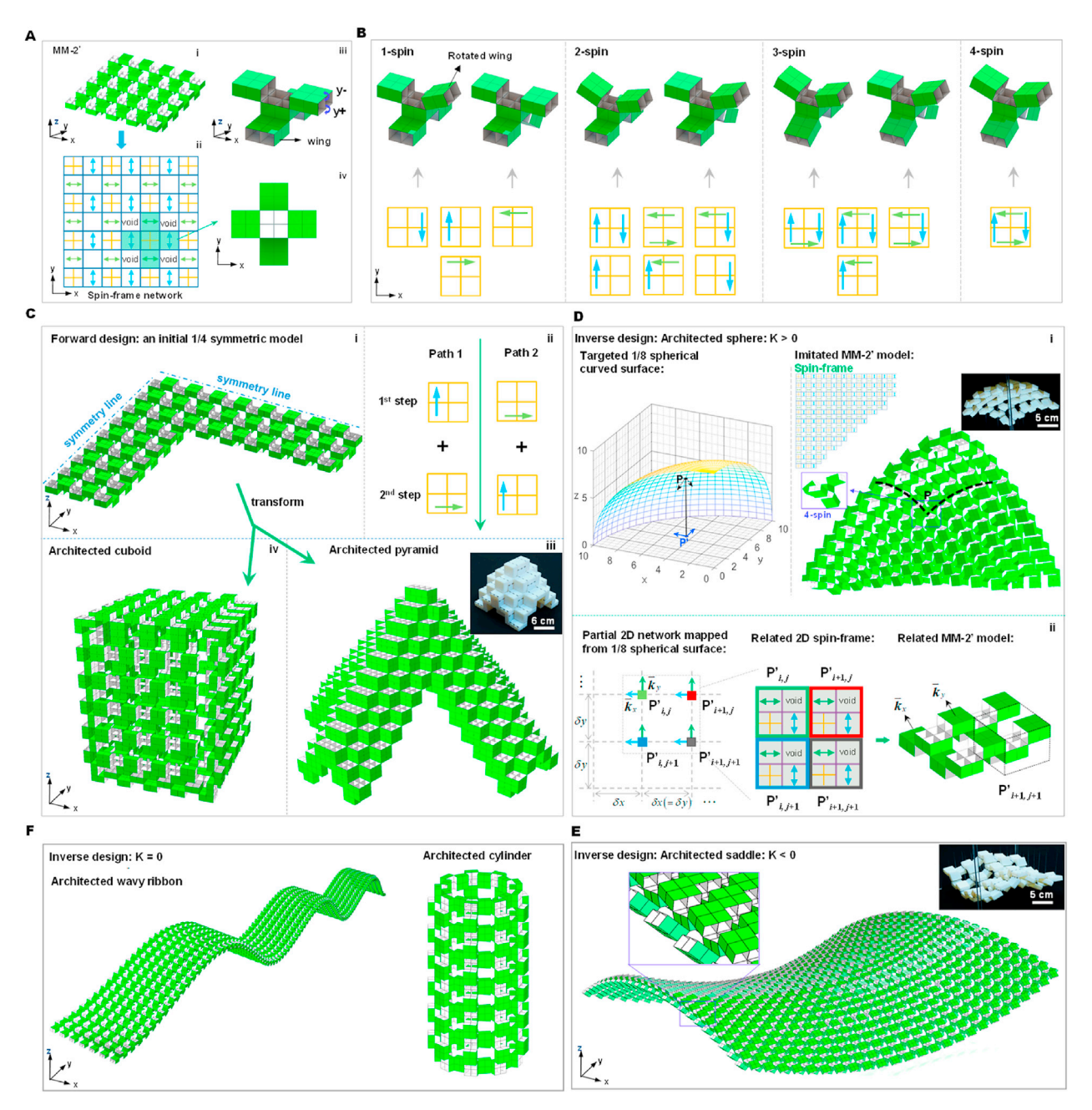


**Fig. 6.** Forward and inverse designs for tessellated surfaces morphing from the pluripotent MM-2' platform. (**A**) Mapping the MM-2' platform (i) to a 2D spin-frame network (ii). (iii) and (iv) are the isometric view and top view of the periodic unit cell, respectively. (**B**) Four different rotated spin frames (1-spin, 2-spin, 3-spin, and 4-spin) by combinatorically rotating either 1, 2, 3, or 4 wings. Top shows the schematic illustration of 3D rotated models in selected spin frames. (**C**) Forward method to generate tessellated pyramid (iii) and cuboidal (iv) shapes from the same initial one-quarter symmetric model through two different sequential kinematic paths. Inset shows the physical prototype. (**D**) Inverse design to imitate 1/8 tessellated spherical shape with Gaussian curvature K > 0 from the pluripotent MM-2' platform whose spin frame details can be seen in Fig. S15A. (i) Left: discretization process of 1/8 spherical shape; Right: imitation of the discretized 1/8 spherical shape with 3D-printed samples; (ii) the partial mapping details from 2D network to spin-frame and finally to MM-2' model. (**E**) The inverse imitated tessellated saddle shape (see also the inserted 3D-printed samples) with Gaussian curvature K < 0 based on the MM-2' platform. (**F**) The inverse imitated tessellated wavy ribbon-like and cylindrical shapes with Gaussian curvature K = 0 based on the MM-2' platform.

# 2.6. Reprogrammable pluripotent matter for architected curved surfaces

The enormous combinatoric structural modes in the periodic MM-2' (Fig. 5F) make it become potential reprogrammable pluripotent matter for further shape morphing into 3D architected surfaces with different curvatures.

#### 2.6.1. Forward design

To explicitly show the reprogrammable shape-morphing process, we map the 3D MM-2' model (Fig. 6A (i)) onto a 2D spin-frame network in xy plane (Fig. 6A (ii)), where the square with "+" symbol represents a non-rotatable base, while its four neighboring squares represent four rotatable side wings around the base. The symbols of " $\uparrow$ ,  $\downarrow$ " and " $\rightarrow$ ,  $\leftarrow$ " represent the directional spin of side wings around the ( $y^+$ ,  $y^-$ ) axis and ( $x^+$ ,  $x^-$ ) axis, respectively. The blank squares denote voids. The free and independent rotation of four

side wings in the 3D unit cells (Fig. 6A (iii)) generates four different combinatoric deployment mechanisms: 1-spin, 2-spin, 3-spin, and 4-spin, where n-spin represents rotating n wings that generate  $C_4^n$  deployment motifs as illustrated in Fig. 6B. Thus, through the combinatoric deployment of different motifs among unit cells in the initial spin pattern, we can achieve a large number of programmable architectures with divergent topologies by following rational kinematic paths.

To demonstrate its programmable shape morphing of MM-2′, starting from the initial cross shape (one quarter of the model is shown in Fig. 6C considering its symmetry around both x- and y-axis), we realize an architected pyramid shape (Fig. 6C (iii)) through the forward design approach (Fig. S14, A to B) with two paths shown in Fig. 6C (ii). Furthermore, the same spin-frame network can also transform into an architected cuboid shape by rationally programming the spin rotation angles (Fig. 6C (iv)). The detailed deployment spin-frame network for achieving the pyramid shape is shown in Fig. S14C, which utilizes four combined spin motifs in the unit cell such as 1-spin (around  $x^+$ ), two 2-spin (around  $x^+$  and  $x^-$ ;  $x^+$  and  $y^+$ ), and 3-spin (around  $x^+$ ,  $x^-$ , and  $y^+$ ).

The kinematic path during the transformation can be quantitatively described by a shape function  $F(\mathbf{R})$ , which takes the general form of:

$$F(\mathbf{R}) = \prod \mathbf{R}_{nx}(\theta_n) \mathbf{R}_{ky}(\theta_k)$$
 [10]

where  ${\bf R}$  is the 3  $\times$  3 right-bottom corner part of the transformation matrix  ${\bf T}_{ij}$  (see Eq. S2 in the *Supplementary Materials*), and  $\Pi$  represents the multiplication operation of matrices.  ${\bf R}_{nx}$  and  ${\bf R}_{ky}$  represent the respective local spin-rotation matrix along the x- and y-axis in each unit cell, which is determined only by its related rotated angles  $0^{\circ} \le \theta_n$ ,  $\theta_k \le 90^{\circ}$  (*Supplementary Materials*). Since each product order represents one deployment path, given the independence of the rotational spins, there are infinite kinematic paths to achieve the target shape by randomly arranging the product order of  ${\bf R}$  in Eq. [10]. Representatively, we decompose the spin motifs into two sequential deployment paths to generate the target pyramid shape: Path 1 with x-spin first followed by y-spin (i.e.,  $F_{\text{Path}-1}({\bf R}) = \sum_{n=1} {\bf R}_{nx} \sum_{k=1} {\bf R}_{ky}$ ) and Path 2 with y-spin first followed by x-spin (i.e.,  $F_{\text{Path}-2}({\bf R}) = \sum_{k=1} {\bf R}_{ky} \sum_{n=1} {\bf R}_{nx}$ ) with  $\theta_n = 90^{\circ}$  and  $\theta_k = 90^{\circ}$  (see Fig. S13 and the virtual model in Fig. S14).

### 2.6.2. Inverse design

Starting from the pluripotent MM-2' platform, we propose an inverse design strategy to identify the prescribed kinematic paths to achieve more complex architected surfaces with different intrinsic curvatures. To approximate a curved surface  $\mathbf{S}$  with nonzero Gaussian curvature K such as the spherical shape (K > 0) in Fig. 6D (i), the inverse design procedure will follow 4 sequential steps as described below.

Firstly, the target 1/8 spherical surface is discretized into a meshed surface by two sets of dissecting planes that are parallel to the xz- and yz-plane in identical intervals. Mapping the curved lines and nodes (i.e., intersection points) in the meshed surface onto xz-plane will produce a periodic 2D network with square-shaped units (see the 2D network in xy-plane in Fig. 6D (i), left). Fig. 6D (i) shows one example of the projection from point  ${\bf P}$  to point  ${\bf P}$ . To clearly show the details of the mapped 2D network, Fig. 6D (ii) (left) shows a representative unit including four projected points of  ${\bf P}'_{i,j}$ ,  ${\bf P}'_{i+1,j}$ ,  ${\bf P}'_{i,j+1}$ , and  ${\bf P}'_{i+1,j+1}$  denoted in different color, where the detailed 2D spin frame is shown in the middle of Fig. 6D (ii). The local curvatures  $(k_x, k_y)$  along the two curved lines at each node of the meshed spherical surface  ${\bf S}$  can be expressed as  $(k_x, k_y) = (\partial {\bf S}/\partial x, \partial {\bf S}/\partial y)$ .

Secondly, given the special relations between the local curvatures  $(k_x, k_y)$  and the rotations of local spins, we will map all the determined local curvatures onto the 2D network. For simplicity, we use the green and blue arrows on the 2D network (left of Fig. 6D (ii)) to represent the curvature vector  $\mathbf{k}_x$  and  $\mathbf{k}_y$  at the projection points.

Thirdly, we will transform the mapped 2D network into a 2D spin frame by replacing all the corresponding projected points with a local spin frame. As illustrated in the related 2D spin frame in Fig. 6D (ii) (middle) for the four points, the two rotatable spins (squares with arrow) will represent two local curvatures, while the non-rotatable part (small square with cross lines) will denote the projected point. Specifically, the projected lines of the 2D network will reduce to the bonds that connect the local spin frames. In this way, we can obtain the entire spin frame for the targeted 1/8 spherical surface. For simplicity, we dissect the 1/8 spherical surface with only 10 intervals along the *x* and *y*-axis, where its spin frame is shown in the top middle inset of Fig. 6D (i) and Fig. S15a-i.

Lastly, we will correlate the obtained spin frame with the deployment of our proposed MM-2' model via n-spin deployment mechanism (see the representative point  $\mathbf{P'}_{i+1,\ j+1}$  in the right two figures of Fig. 6D (ii)). The target architected shape will be obtained by rotating all local wings of the determined MM-2' model with certain angles in terms of their corresponding two local curvatures at each discretized node.

The right of Fig. 6D (i) shows the obtained architected spherical surface from MM-2' via the proposed inverse design (see the related spin rotation angles for each discretized point in Table S1). In principle, by following the generalized inverse design strategy, starting from the same pluripotent MM-2' platform, we can achieve any curved surface shape with arbitrary intrinsic curvature. Representatively, we demonstrate the generation of more varieties of architected curved surfaces such as a saddle shape with negative Gaussian curvature (K < 0) in the functional form of  $S = x^2 - y^2$  ( $0 = x, y \le 1$ ) (Fig. 6E, spin rotation angles are listed in Table S2), ellipsoidal shapes, wavy ribbon, and cylindrical shapes shown in Fig. 6F and Fig. S15b.

To validate the forward and inverse imitation capability of the MM-2', we experimentally assemble one MM-2' base pattern through multi-material 3D printing (see Fig. S16 and details in the *Supplementary Materials*), and demonstrate its deployment into a pyramid, spherical (partially), and saddle shape (insets in Fig. 6C (iii), Fig. 6D and 6E). We note that no structural collision occurs during the deployment. Given the fact that the two sets of dissecting planes are parallel with identical intervals, the rotation angles of the rotated wings located on the same dissecting planes will be the same (see Table- S1 in spherical surface imitation for example), which ensures compatible deformation in all the rotated wings during the target shape imitation.

Based on the inverse design strategy, varieties of geometries in different 3D shapes can be achieved from the flat, quasi-3D base pattern, including prismatic shapes and curved surfaces such as cylindrical, spherical, elliptical, paraboloid, and conical shapes. Despite the promise, it has certain limitation on the achievable 3D shapes. For example, some special shapes or topological changes cannot be achieved via our proposed strategy, including star polyhedron with sharp extrusions, toroid shapes with a hole in the middle, and hyperboloid and helicoid shapes etc.

### 3. Discussions and conclusions

We exploit utilizing the kinematic bifurcation in mechanism to achieve largely enriched mobilities, enhanced reconfigurability, and reprogrammability in the example system of 3D kirigami-inspired architected matter. It lays a theoretical foundation for

designing reconfigurable and shape-reprogrammable materials with evolving shape-morphing features. We uncover the kinematics underpinning its multiple transformation modes including the kinematic bifurcation through the developed models. Rational designs of building blocks enable their frustration-free and periodic planar tessellation with encoded non-bifurcated/bifurcated transition modes. We demonstrate leveraging kinematic bifurcation for achieving the mapping from one design to many structural configurations. Moreover, the bifurcated structure provides a pluripotent platform to be reprogrammed into multiple architected curved surfaces through both forward and inverse designs.

The 3D kirigami-inspired modules largely free the constrained structural mobilities in conventional kirigami designs of planar thin sheets [15,25,26]. We note that the 3D kirigami-inspired approach could be generalized to generate more derived transformable modules [35]. Considering the four connection ways between two neighboring cubes, the 3D kirigami-inspired modules consisting of 4, 6, and 8 cubes in Fig. 2A-C could further evolve into  $4^4 = 256$ ,  $4^6 = 4,096$ , and  $4^8 = 65,536$  derived modules by manipulating combinatorial designs of the cube connections, respectively. Furthermore, more complex 3D modules can be constructed by combining the three basic modules, e.g., 12-cube modules by combining the units of 4 cubes and 8 cubes in Fig. 2. However, it does not necessarily result in more structural reconfiguration modes and more bifurcated kinematic paths compared to the 8cube module (Fig. S17), which depends on how the cubes are connected in a symmetric or asymmetric way.

Given the scale and materials independent mechanism design, the intriguing shape-evolving characteristics of the 3D kirigamiinspired architected matter could find potential applications in reconfigurable mechanical metamaterials and morphing architectures. For practical applications, load-carrying capacity is one of the important parameters that need to be considered for the proposed reconfigurable structures. We note that most of the transformed architectures of our proposed designs are stable and capable of carrying certain external loads, as demonstrated by the three representative architectures connected through plastic tapes as free-rotational hinges in Fig. 7A. We find that the for the architectures that could be treated as rigid structures connected through rigid bonds (see the free body diagram in the lower inset of Fig. 7A), they can tolerate much higher loads (e.g., a 60 lb kettlebell on top in Fig. 7A (i)). However, the arc-like architectures show lower load capacity (e.g., 10 lb dumbbell on top in Fig. 7A (ii-iii). As schematically illustrated in Fig. 7A (iv) on the free body diagram in both xzand yz-plane of the architecture in Fig. 7A (iii), the loading capacity of the arc-like architectures depends on the ground friction force, the bonding between hinges and cubes, and the composed materials stiffness in the hinges. Fig. 7A (iii) shows that given a large enough friction force, most of the applied external load will be mainly transferred to and tolerated by the joint hinges that connect different layers and the related cube-hinge bonds (see the bonds with loaded hinges highlighted in yellow colors). However, for the curved architected structures, load-bearing hinges that can resist bending moment are required to connect the curved structures for

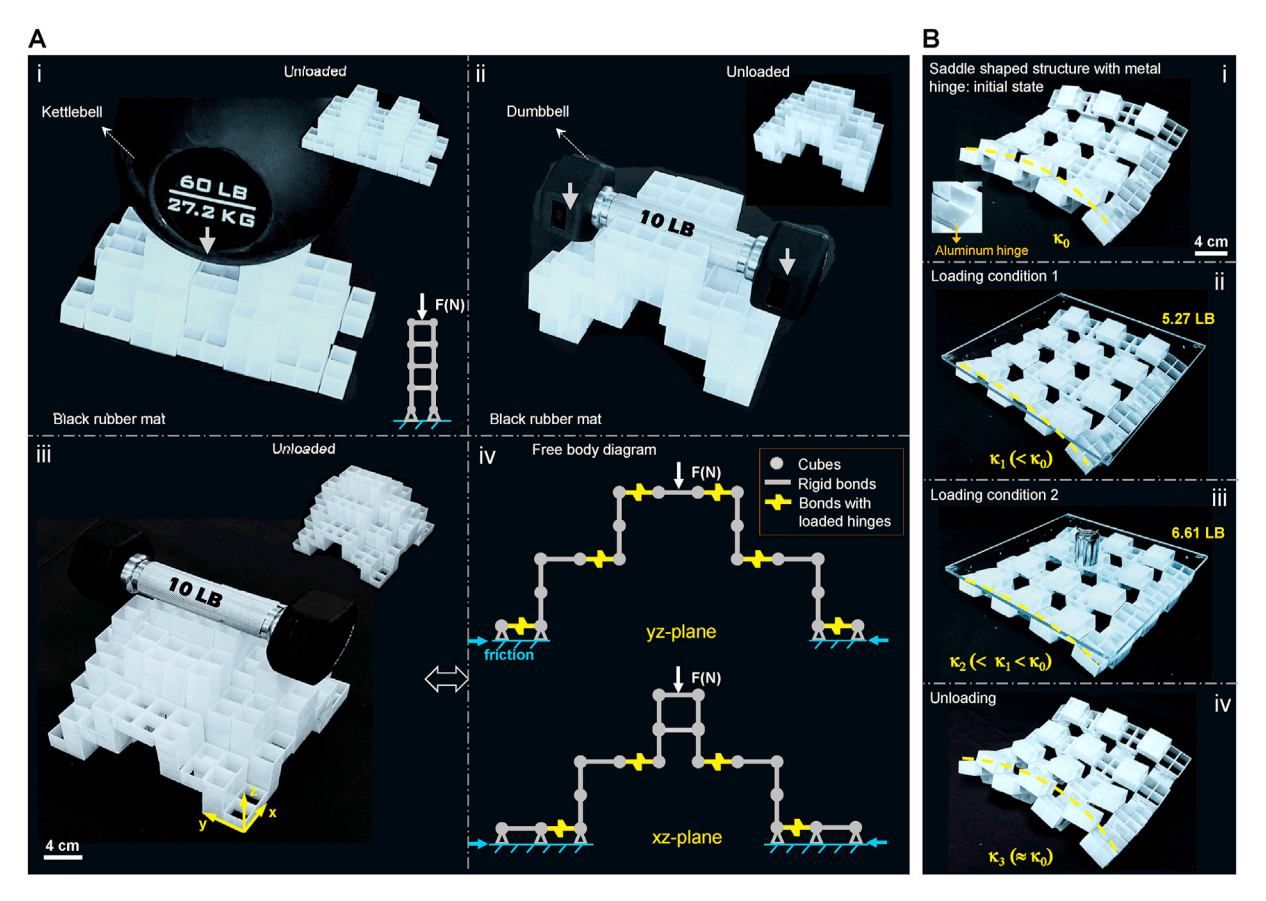


Fig. 7. Loading capacity of selected reconfigured architectures. (A) Examination of loading capacity of three representative architectures: (i) Building-6 in Fig. 5F(i) with a 60 lb kettlebell placed on top; (ii) Building-7 in Fig. 5F(ii) and (iii) Pyramid structure in Fig. 6C(iii) with a 10 lb dumbbell placed on top. The top-right insets show the unloaded configurations. (iv) The free body diagram of architecture in (iii). (B) Saddle shaped structure connected through aluminum hinges. (i) Initial state; (ii) deformed state under loading condition 1 with an acrylic plate of 5.27 lb placed on top; (iii) Further deformed state under loading condition 2 with increased load of 6.61 lb on top; (iv) recovered structure from unloading in (iii).

carrying external loading; otherwise, they will collapse via free rotation of the hinges. To demonstrate it, we use thin aluminum plates as connection hinges (Fig. 7B (i)) and show that the curved saddle-like structure can support about 6 lb external load with a decreased curvature (Fig. 7B (ii-iii)). After unloading, the curvature of the curved structure almost returns to its original value before loading (Fig. 7B (iv)).

Meanwhile, control and actuation of deployment will be important considering their rich mobilities, especially at the bifurcation points for a desired transition pathway. Exclusive linear kinematic paths for target shapes (e.g., the linear path in Fig. S13) will be needed for easy control of hinge rotating with motion actuators such as motors [47] or other stimuli-responsive actuators [48]. As demonstrated in Fig. 3B, despite multiple transition pathways at the bifurcated points, a certain desired path for a target shape change is possible by tuning the specified dihedral folding angle between different cubes. Thus, to achieve a target transition pathway via actuation, the revealed kinematics modeling could provide important guidance for appropriate sequential actuations of the specified folding angles.

#### 4. Materials and methods

Details of fabrication of prototypes and assembly, kinematics analysis, transitions of building blocks and their tessellation, kinematic mobility, and forward and inverse designs are described in Supplementary Materials.

#### **Author contribution**

Y. L. and I. Y. proposed and designed the research, Y. L. designed and fabricated the prototypes and performed theoretical analysis of the system. Y. L. and J. Y. wrote the manuscript.

#### **Funding**

The authors acknowledge the funding support from National Science Foundation, United States, under award number CMMI CAREER-2005374.

### Data and materials availability

All data is available in the main text or the supplementary materials.

#### **Declaration of competing interest**

The authors declare that they have no known competing financial interests or personal relationships that could have appeared to influence the work reported in this paper.

#### **Acknowledgments**

The authors thank Sid Collins for artistic inspiration.

## Appendix A. Supplementary data

Supplementary data to this article can be found online at https://doi.org/10.1016/j.mtphys.2021.100511.

#### References

- [1] S.C. Goldstein, et al., Computer 38 (6) (2005) 99.
- [2] K. Oliver, et al., J. Mater. Sci. 51 (24) (2016) 10663.
- [3] H. Ko, A. Javey, Acc. Chem. Res. 50 (4) (2017) 691.
- T. van Manen, et al., Mater. Today 21 (2) (2018) 144.
- [5] K. Bertoldi, et al., Nature Reviews Materials 2 (11) (2017) 17066.
- [6] M. Yim, et al., IEEE Robot. Autom. Mag. 14 (1) (2007) 43.
- [7] S. Barbarino, et al., J. Intell. Mater. Syst. Struct. 22 (9) (2011) 823.
- [8] F. Momeni, et al., Mater. Des. 122 (2017) 42.
- [9] S.J.P. Callens, A.A. Zadpoor, Mater. Today 21 (3) (2018) 241.
- [10] X. Ning, et al., Advanced Materials Interfaces 5 (13) (2018) 1800284.
- [11] Y. Chen, et al., Science 349 (6246) (2015) 396.
- [12] R.J. Lang, et al., Appl. Mech. Rev. 70 (1) (2018).
- [13] E.A. Peraza-Hernandez, et al., Smart Mater. Struct. 23 (9) (2014): 094001.
- [14] N. Turner, et al., Proc. IME C J. Mech. Eng. Sci. 230 (14) (2016) 2345.
- [15] Y. Cho, et al., Proc. Natl. Acad. Sci. Unit. States Am. 111 (49) (2014) 17390.
- [16] D.M. Sussman, et al., Proc. Natl. Acad. Sci. Unit. States Am. 112 (24) (2015) 7449
- [17] M.K. Blees, et al., Nature 524 (7564) (2015) 204.
- [18] T.C. Shyu, et al., Nat. Mater. 14 (8) (2015) 785.
- [19] R.M. Neville, et al., Sci. Rep. 6 (1) (2016) 31067.
- Y. Tang, et al., Adv. Mater. 29 (10) (2017) 1604262.
- [21] Y. Yang, et al., Physical Review Materials 2 (11) (2018) 110601.
- [22] D.-G. Hwang, M.D. Bartlett, Sci. Rep. 8 (1) (2018) 3378
- [23] Y. Tang, et al., Proc. Natl. Acad. Sci. Unit. States Am. 116 (52) (2019) 26407.
- [24] E.D. Demaine, J. O'Rourke, Geometric Folding Algorithms: Linkages, Origami, Polyhedra, Cambridge University Press, 2007.
- [25] Y. Tang, J. Yin, Extreme Mechanics Letters 12 (2017) 77.
- [26] J.N. Grima, K.E. Evans, J. Mater. Sci. Lett. 19 (17) (2000) 1563.
- [27] G.P.T. Choi, et al., Nat. Mater. 18 (9) (2019) 999.
- [28] A. Rafsanjani, K. Bertoldi, Phys. Rev. Lett. 118 (2017): 084301.
- [29] L.H. Dudte, et al., Nat. Mater. 15 (5) (2016) 583.
- [30] P. Dieleman, et al., Nat. Phys. 16 (1) (2020) 63.
- [31] T. Castle, et al., Science Advances 2 (9) (2016): e1601258.
- [32] J.T.B. Overvelde, et al., Nat. Commun. 7 (1) (2016) 10929. [33] J.T.B. Overvelde, et al., Nature 541 (7637) (2017) 347.
- [34] N. Yang, J.L. Silverberg, Proc. Natl. Acad. Sci. Unit. States Am. 114 (14) (2017)
- [35] Y. Li, et al., Adv. Funct. Mater. (2021) 2105641.
- [36] P. Blanchard, et al., Differential Equations, Thompson, London, 2006.
- [37] B. Davide, Nonlinear Solid Mechanics: Bifurcation Theory and Material Instability, Cambridge University Press, 2012.
- [38] Y. Chen, et al., Int. J. Solid Struct. 42 (8) (2005) 2287.
- [39] P. Kumar, S. Pellegrino, Int. J. Solid Struct. 37 (46) (2000) 7003.
- [40] T. Tarnai, Kinematic bifurcation, in: S. Pellegrino (Ed.), Deployable Structures, Springer Vienna, Vienna, 2001, p. 143.
- https://erikdemaine.org/thok/flexcube.html.
- [42] J.W. Truman, L.M. Riddiford, Nature 401 (6752) (1999) 447.
- [43] S. Kriegman, et al., Proc. Natl. Acad. Sci. Unit. States Am. 117 (4) (2020) 1853.
- [44] J. Denavit, R.S. Hartenberg, J. Appl. Mech. 22 (1955) 215.
- [45] W.W. Gan, S. Pellegrino, Proc. IME C J. Mech. Eng. Sci. 220 (7) (2006) 1045.
- [46] C. Coulais, et al., Nature 535 (7613) (2016) 529.
- [47] B. Vanderborght, et al., Robot. Autonom. Syst. 61 (12) (2013) 1601.
- [48] Y. Liu, et al., Prog. Polym. Sci. 52 (2016) 79.